INSTITUTE OF PHYSICS PUBLISHING PLASMA SOURCES SCIENCE AND TECHNOLOGY
Plasma Sources Sci. Technol. **14** (2005) 51–60 doi:10.1088/0963-0252/14/1/007

Space and time resolved rotational state populations and gas temperatures in an inductively coupled hydrogen RF discharge

M Abdel-Rahman[1], T Gans[2], V Schulz-von der Gathen[1,3] and H F Döbele[1]

[1] Institut für Laser- und Plasmaphysik, Universität Duisburg-Essen, Campus Essen, 45117 Essen, Germany
[2] Institut für Plasma- und Atomphysik, Ruhr-Universität Bochum, 44780 Bochum, Germany

E-mail: svdg@uni-essen.de

Received 26 July 2004
Published 12 January 2005
Online at stacks.iop.org/PSST/14/51

Abstract
Gas temperature is of major importance in plasma based surface treatment, since the surface processes are strongly temperature sensitive. The spatial distribution of reactive species responsible for surface modification is also influenced by the gas temperature. Industrial applications of RF plasma reactors require a high degree of homogeneity of the plasma in contact with the substrate. Reliable measurements of spatially resolved gas temperatures are, therefore, of great importance. The gas temperature can be obtained, e.g. by optical emission spectroscopy (OES). Common methods of OES to obtain gas temperatures from analysis of rotational distributions in excited states do not include the population dynamics influenced by cascading processes from higher electronic states. A model was developed to evaluate this effect on the apparent rotational temperature that is observed. Phase resolved OES confirmed the validity of this model. It was found that cascading leads to higher apparent temperatures, but the deviation ($\simeq$25 K) is relatively small and can be ignored in most cases. This analysis is applied to investigate axially and radially resolved temperature profiles in an inductively coupled hydrogen RF discharge.

1. Introduction

RF-excited discharges are finding widespread application in the field of surface modification in connection with semiconductor production and thin film deposition [1]. Plasmas with working gases containing hydrogen are widely used in the field of material treatment; pure hydrogen plasmas are applied in microelectronics for surface cleaning and etching [2]. For these applications inductively coupled plasmas (ICPs) have several advantages compared to capacitively coupled radio frequency (CCRF) discharges. Homogeneity of the discharge is of major concern for all these technological applications. Gradients along the surface to be modified influence the efficiency of the processes and have to be controlled to stay within specified limits. The gas temperature, i.e. the translational temperature of the gas can limit a specific plasma chemical process and its applicability in the case of temperature sensitive materials and can influence, in addition, other important discharge parameters such as the degree of dissociation and particle densities. A knowledge of the gas temperature distribution within the ICP and in particular close to the surface is, therefore, of great importance for the application.

[3] Author to whom any correspondence should be addressed.

Infrared absorption, laser-induced fluorescence and optical emission spectroscopy (OES) are commonly used techniques to measure temperatures of excited or ground state species in gas discharges [3, 4]. OES is a convenient and non-intrusive diagnostic tool, well suited for the determination of important plasma parameters such as particle densities, particle temperatures and electron energy distributions, as well as for the determination and control of the gas temperature [5–7]. The most common experimental technique for determining the gas temperature is the analysis of the intensity distribution in the rotational bands of electronic transitions [8]. The rotational population $N(N')$ of a vibrational sequence (v') of an electronically excited state is mostly well characterized by an excited state rotational temperature $T_{\mathrm{rot}}(v')$ that reflects the gas temperature under certain conditions. N' and v' indicate the respective rotational and vibrational quantum numbers. T_{rot} is obtained either by using the 'Boltzmann-plot-technique' or by a comparison of measured spectra with simulations based on the appropriate molecular constants [9]. In the following, we will call the temperature determined by this procedure from excited state emission simply the 'temperature' or 'rotational temperature'. The agreement between the rotational temperature and the gas, i.e. the translational, temperature has to be proved. The Fulcher-α bands of the $3p^3$ state of H_2 are often used for this purpose. These rotational lines are located in a convenient spectral range (around 600 nm) and are relatively intense—easily recordable with common photodetectors.

A basic problem of emission spectroscopy is the need to draw conclusions on ground state populations and related properties from the measured emission out of excited states. In the case of gas temperature measurements, the determination of rotational and vibrational populations of the excited molecular bands is necessary. It was shown recently [10, 11] that by combining sophisticated techniques like phase resolved OES (PROES) and modelling, this basic problem of OES can be overcome and that quantitative information referring to the ground state can be retrieved.

PROES measurements of rotational distributions on a time scale of some nanoseconds, as requested for the usually applied excitation frequencies of 13.56 or 27.12 MHz, are not trivial due to the comparatively low light level of single molecular lines of higher quantum number N' and the dynamic range required by intensity variations within an excitation cycle. With a special intensified charged coupled device (ICCD) matrix camera (LaVision Picostar HR), it is possible to acquire information from every RF-cycle [10]. This reduces measurement times by a factor of 1000 as compared to standard ICCD cameras. The results of Gans *et al* [10] by PROES showed that in CCRF discharges strong dynamic effects influence the population of the electronically excited hydrogen states.

Furthermore, time-integrated measurements showed that these discharges exhibit strong radial dependences of electron and particle densities as well as of gas temperature [4, 12, 13]. Measured OES intensities result from line-of-sight integration along the optical path, so that the determination of spatially resolved quantities necessitates a deconvolution procedure [14]. For a cylindrically symmetric situation, the well-known Abel inversion can be used to reconstruct the radial gas temperature profiles [12]. Blades and Horlick [15, 16] used this technique for the calculation of radial emission profiles in ICP torches.

Unlike the case of CCRF discharges the population dynamics has not been studied in ICPs so far. We will discuss phase and space resolved measurements of rotational populations in this type of discharges applying Abel inversion of phase resolved emission spectroscopic data.

2. The experimental set-up

The experimental layout, including the optical detection assembly, is shown in figure 1. The water cooled discharge vessel has a diameter of 30 cm and a height of 40 cm. In the central plane the chamber is equipped with four large (CF-150) ports displaced by 90°. Two of them are equipped with

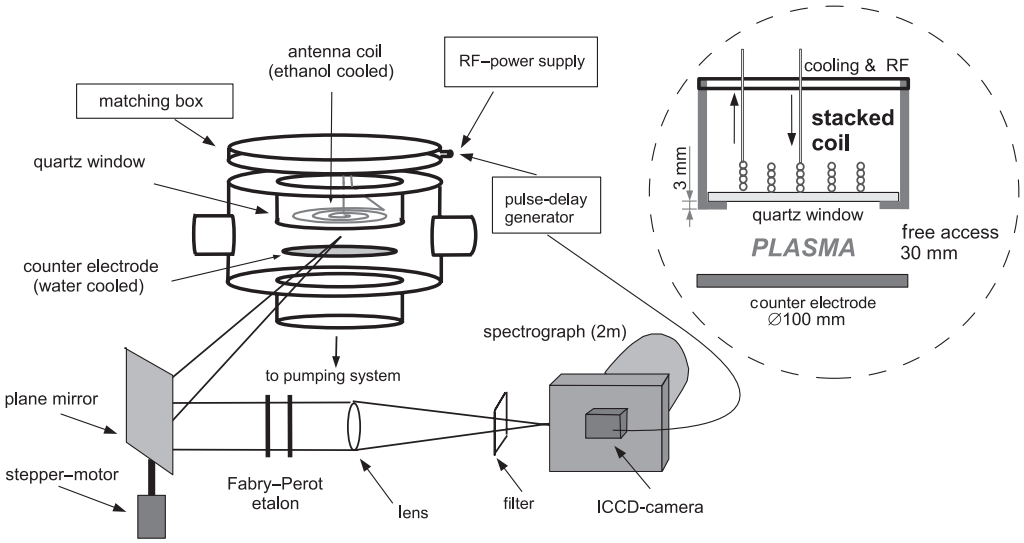

Figure 1. Experimental set-up including the optical system. The insert shows the coil–electrode system in more detail.

fused silica windows for OES and other optical diagnostics. The other flanges allow the introduction of carriers for the electrode plate (see below) and feed-throughs, e.g. for a Langmuir probe system. The chamber is evacuated to a base pressure of below 10^{-4} Pa. The working gas is premixed (H_2/He/Ne/Ar/Kr: 95/2/1.5/1/0.5) and injected into the vessel through a mass flow controller (Tylan) attached to another smaller port positioned in a lower plane. The mixture is chosen in order to determine additional quantities characterizing the plasma, such as the degree of dissociation and the electron energy distribution function (EEDF). These measurements will be the subject of forthcoming publications, currently in preparation. No deviation of the Fulcher line intensities was observed as compared to a pure hydrogen discharge. A stainless steel carrier in the top port positions a quartz window of 4 mm thickness and 100 mm diameter 20 mm above the central diagnostic plane. The window separates the vacuum and the plasma from the planar spiral RF induction coil in air. There is no Faraday shield placed between the coil and the quartz window. Due to this holder an axial range of about 3.5 mm just below the dielectric quartz window is optically not accessible as sketched in the insert in figure 1.

The five-turn coil, also indicated in this figure, with an outer diameter of 80 mm, is made of a band of four copper tubes stacked on each other and is cooled from inside with ethanol. The RF-power is fed to the antenna through a matching network that is directly positioned on top of the chamber to minimize losses. The source is powered at 13.56 MHz using an ENI OEM-12A radio frequency power generator. The effective operating power of 150–350 W is measured as the difference between forward power P_{for} and reflected power P_{ref}, directly, with the power meter of the power supply.

A stainless-steel lower electrode of diameter 100 mm—water-cooled and grounded—is mounted below the coil parallel to the quartz window. The optically accessible axial distance between this lower electrode and the dielectric quartz window is 30 mm.

The determination of temperature profiles with both axial and radial space resolution requires the installation of an optical system able to record 'side-on' projected intensities at various lateral positions. The light emitted from the discharge is imaged and scaled down with a combination of a rotatable plane mirror ($100 \times 100\,\text{mm}^2$) and a lens ($f = 450$ mm) onto the entrance slit of a 2-m-spectrograph (Jenoptik PGS 2, inverse dispersion $0.34\,\text{nm}\,\text{mm}^{-1}$ with a $1302\,\text{grooves}\,\text{mm}^{-1}$ grating). This results in a maximum diameter of an optical chord of about 1 mm within the discharge. A fast gated ICCD camera (LaVision Picostar HR) with an active image matrix of 13.2 mm × 8.8 mm (576 × 384 pixel) is used as the detector. On this area the slit image represents an axial cross-section of the discharge (first dimension). In the transverse direction a spectral interval of ∼4.5 nm can be recorded, in which the first five lines of a hydrogen Fulcher rotational band can be accommodated. A lateral scan of this axial cross section transverse through the discharge with the aid of the rotatable mirror yields the second dimension of observation (figure 2). The rotation is controlled by a stepper motor. The accessible lateral distance from the central axis is limited by the observation window to 70 mm. The complete optical system was calibrated with a tungsten ribbon lamp between 350 and 750 nm.

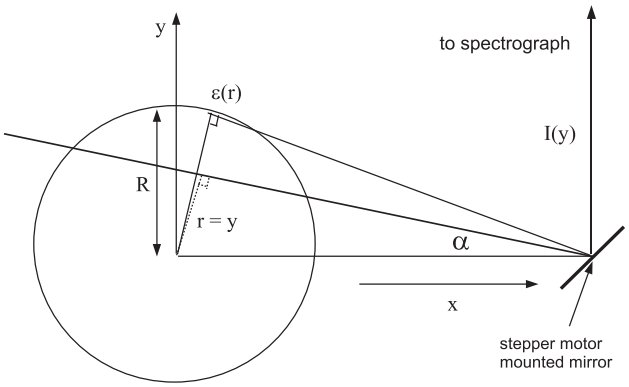

Figure 2. Rotatable mirror for Abel inversion.

For a series of measurements, a Fabry–Perot interferometer (FPI, Burleigh RC-150) was installed in the optical path.

The camera allows the integration of the emission signal taken with a time gate of 3 ns width at a repetition rate as high as 13.56 MHz so that each individual RF-cycle can contribute. For phase-resolved measurements the gate is locked to a fixed phase position within the exciting RF-cycle. With a variable delay between the fixed phase and the gate the complete RF-cycle of 74 ns is covered with 25 time windows. This allows PROES measurements, even of low intensity lines, of higher rotational quantum number N' in a time sufficiently short (<5 min), such that stable experimental conditions can be assumed safely.

2.1. Measuring procedure of phase resolved and radially and axially space resolved rotational temperature profiles

In order to obtain time resolved rotational temperatures with axial and radial space resolution the following procedure was applied: the radius of the discharge was scanned with the stepper-motor controlled mirror over 12 measurement positions starting at the centre of the discharge. By using the stepper motor our measurement is in principle based on an angular displacement. We took account of this by transforming the angle α for the known distance between mirror axis and discharge axis into the lateral distance y of a line-of-sight (see figure 2) while preparing the numerical integration applied for Abel inversion with the Fourier method [17, 18]. At each angular position the spectrum of the ($v = 2$) Q-branch Fulcher-α rotational lines (see figure 3) was recorded simultaneously in 25 time windows covering the complete excitation cycle. At each angular and each time position the axial intensity profile—on the second dimension of the ICCD-camera—is subdivided into 24 equidistant axial positions to keep the amount of data manageable. To further reduce the data, the intensities of each of the five Q-branch lines analysed are extracted from the spectrum and stored in separate files. Finally, the time and space (two dimensions) resolved intensities of the five Fulcher lines are stored in sets of 12 (radial positions) × 5 (spectral lines) files for further analysis—each of the files containing a matrix of 25 time windows and 24 axial positions. Abel inversion routines are then applied to each set of axial and temporal intensity measurements of the five Fulcher lines. The radial emissivity

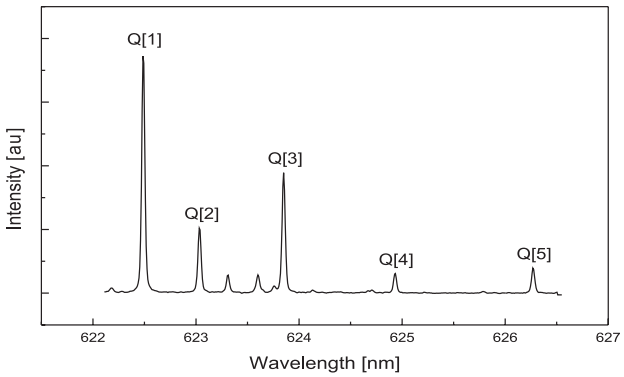

Figure 3. Spectrum of the first five rotational lines ($N = 1$–5) of the Q-branch ($\Delta N = 0$) of the $v = 2$ Fulcher-α emission band of hydrogen.

results are stored in another set of 12 separate files with the same dimensional partition as before for each line. For each of these temporal, axial and radial positions the rotational temperature routine is applied to the five Q-branch emissivities to yield the respective rotational temperatures at each spatial and temporal position.

3. Determination of rotational temperature

The determination of the rotational temperature is based on the observation of rotational line intensity distributions in the vibronic bands of the Fulcher-α band system. The Q-branch transitions ($\Delta N = 0$) of the diagonal bands ($\Delta v = 0$) of the Fulcher-α system ($3p\,^3\Pi_u^- \rightarrow 2s\,^3\Sigma_g^+$ electronic transition) are recorded. The Q-branches of the Fulcher-α band system are frequently used in plasma diagnostics, since the rate coefficients in the adiabatic approximation can be applied [19]. We selected the usual vibrational $v = 2$ Fulcher-α band, because this band has no overlap with other emission lines. A knowledge of the intensity ratios within one rotational band is necessary to infer the rotational temperature, and it is advantageous to measure the intensities of the rotational lines simultaneously in order to avoid the influence of time dependent drifts of the plasma or of the experimental conditions [10].

It is possible to record a sufficient section of a rotational band (five rotational lines) in one spectral image with our detection system (see figure 3). The measured intensities of the first five Q-branch (2-2) Fulcher-α rotational lines differ within one spectrum by at least a factor of ten so that a detection system with a high dynamic range is necessary, if the calculation of the rotational temperature is to be inferred from one single record. The effective dynamic range of our camera system of about 14 bits is sufficient for this task, in view of the plasma background. Since the relative error of the low-intensity molecular lines is larger than that for the more intense lines, no linear fit was applied to obtain the temperature from a Boltzmann plot, but the least-squares deviation between the calculated and the measured intensities was used instead, so that all rotational lines contribute according to their intensity. The analysis applied to infer the rotational temperature is explained in detail elsewhere [10, 19].

3.1. Rotational temperatures of the $3p\,^3\Pi_u^- \rightarrow 2s\,^3\Sigma_g^+$ *states of* H_2

To summarize the basis of this diagnostic, it is useful to recall that the intensity of a spectral line due to a ($n'v'N' \rightarrow n''v''N''$) ro-vibronic transition can be written as the product of the population density of the upper state $N_{n'v'N'}$ and the Einstein transition probability for spontaneous emission $A^{n'v'N'}_{n''v''N''}$:

$$I^{n'v'N'}_{n''v''N''} = N_{n'v'N'} A^{n'v'N'}_{n''v''N''},$$

where a single prime is used to denote quantities pertaining to the upper level (in emission it is the initial state) and double primes for the lower level (the final state in emission). $n'^{,''}$, $v'^{,''}$ and $N'^{,''}$ are quantum numbers of electronic, vibrational and rotational (total angular momentum without electronic spin) levels, respectively. If the population of one rotational band of the upper state can be described by a Boltzmann distribution, then the rotational temperature $T_{\mathrm{rot}}(n', v')$ can be obtained from the relation

$$N_{n'v'N'} = c_{n'v'} g_{\mathrm{as}} (2N' + 1) \exp\left(-\frac{E_{n'v'N'}}{k_{\mathrm{B}} T_{\mathrm{rot}}(n'v')}\right),$$

where $c_{n'v'}$ is a normalizing constant, g_{as} the degeneracy caused by the nuclear spin, $E_{n'v'N'}$ the energy of the ro-vibronic level, k_{B} the Boltzmann constant and T_{rot} the rotational temperature. A detailed discussion of the conditions required for the relation between the rotational line intensity distribution and the gas temperature to hold was given by Gans *et al* [10], on the basis of a kinetic model for the population and depopulation of the excited levels involved. The most important assumptions are:

(a) The population distribution in the ground state $1s\,^1\Sigma_g^+$ is determined by heavy particle collisions and obeys a Boltzmann distribution whereby the ground state rotational temperature $T_{\mathrm{rot,g}}$ equals the gas temperature.
(b) The excited states are populated only via electron collisional excitation out of the ground state.
(c) The effective lifetimes of the excited states are independent of the rotational quantum number and are much shorter than the relaxation time of the rotational levels.

The thermal rotational distribution of the electronic ground state $1s\,^1\Sigma_g^+$ is 'copied' into the excited state $3p\,^3\Pi_u^-$ without change of the rotational quantum number N under these conditions. The rotational distribution of the excited state can be determined from the spontaneous emission into the lower state $2s\,^3\Sigma_g^+$. A fit of a Boltzmann distribution to these emissions yields the rotational temperature that is directly connected to the gas temperature under these assumptions.

In the publication mentioned above [10] the influence of cascading processes from higher lying electronic states on the population dynamics of the $3p\,^3\Pi_u^-$ state was analysed. The largest contributions issue from the 4d states so that according to the selection rules Q-transitions from the $4d\,^3\Sigma_g^+$, $4d\,^3\Pi_g^+$ and $4d\,^3\Delta_g^+$ states, and P- and R-transitions, i.e. with change of the rotational quantum number out of the $4d\,^3\Pi_g^-$ and $4d\,^3\Delta_g^-$ states have to be taken into account. The dependence of the cascade contributions on the rotational quantum number N' is determined by the transition probabilities from the

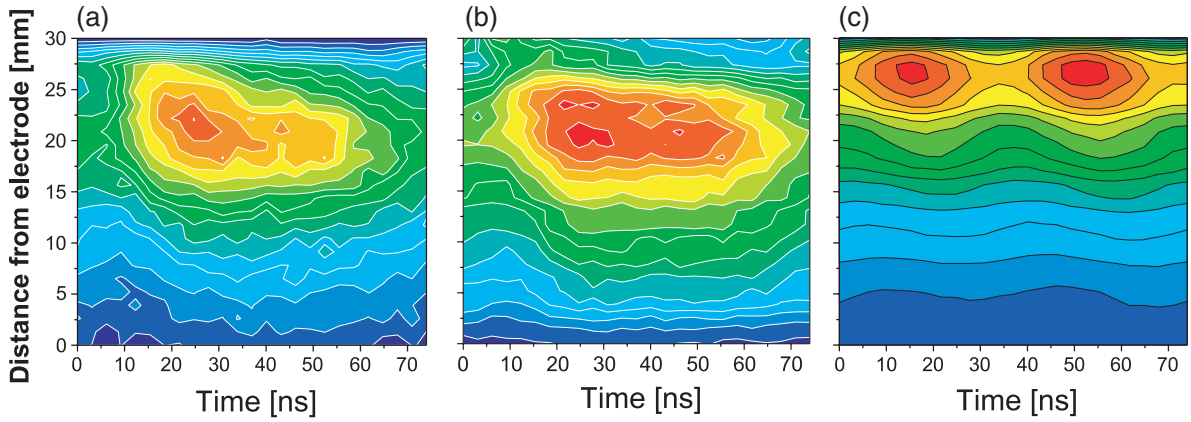

Figure 4. Time resolved axial intensity profile of the Q(1) emission line at 15 Pa for different input powers of (*a*) E-mode (100 W), (*b*) transitional mode (150 W) and (*c*) H-mode (350 W) on the axis of the discharge. Intensities are normalized. Red indicates the highest intensity and blue the lowest one. The intensity in (*c*) is about a factor of 100 higher than in (*a*) and (*b*). The time axis shows one RF-cycle of about 74 ns duration at 13.56 MHz.

4d into the 3p states and by the rotational distribution in the 4d states. The transition probabilities can be described by the Hönl–London factors in the absence of quenching. Neglecting further cascades, the rotational population of the 4d states by electron collisional excitation out of the ground state can be described by

$$n_{n',v',N'} \propto Y_{n'\leftarrow n''}(T_g, N') \cdot g_{a,s} \cdot (2N'+1) \times \exp\left(-\frac{N' \cdot (N'+1) \cdot B_0}{k_B \cdot T_g}\right).$$

Here, B_0 is the rotational constant of the ground state and $Y_{n'\leftarrow n''}(T_g, N')$ describes the dependence of the excitation rates on the rotational quantum number. $Y_{n'\leftarrow n''}(T_g, N')$ depends on the electronic state and can be represented by the Wigner 3-j symbols for the different states. We have to distinguish between states where $\Delta N = 0$ is valid for allowed transitions and the states $4d\,^3\Pi_g^-$, $4d\,^3\Delta_g^-$ for which $\Delta N = \pm 1$ is valid. For the first case $Y_{n'\leftarrow n''}(T_g, N')$ describes the different weightings for transitions of different rotational states that yield a redistribution in the upper state. In the latter case we get two contributions due to the change in the rotational quantum number making the redistribution quite obvious:

$$Y_{n'\leftarrow n''}(T_g, N') = (2N'-1)\begin{pmatrix} N' & 2 & N'-1 \\ -\Lambda' & \Lambda' & 0 \end{pmatrix}^2 \times \exp\left(\frac{2N' \cdot B_0}{k_B \cdot T_g}\right) + (2N'+3)\begin{pmatrix} N' & 2 & N'+1 \\ -\Lambda' & \Lambda' & 0 \end{pmatrix}^2 \times \exp\left(-\frac{(2N'+2) \cdot B_0}{k_B \cdot T_g}\right),$$

Λ' is the angular momentum along the inter-nuclear axis of the excited state. The 'zero' within the 3-j symbol results from the $\Lambda'' = 0$ of the ground state. The '2' is valid for the transition from 1s to 4d. The changes of the population distribution described by this $Y_{n'\leftarrow n''}(T_g, N')$ in combination with a different lifetime of the cascading states result, finally, in rapid variations of the rotational distribution that are attributed to apparent changes of the rotational temperature.

4. Experimental results and discussion

4.1. Time and axial dependences of emission intensities

It was demonstrated in an earlier publication that in a CCRF discharge the electron distribution function is modulated with the RF frequency in a characteristic manner. Our optical detection system is fast enough to follow this time dependence [10].

This modulation of the emitted radiation is also observed in the hydrogen ICP for both well-known modes—capacitive (E-) and inductive (H-) modes. The ICP ignites capacitively (E-mode) with increasing power and evolves gradually into the inductive (H-) mode. A transitional mode is noticeable in between, as shown in figure 4 for the Q(1) line (i.e. Q-branch, $N' = 1$). The same behaviour is observed for all of the Fulcher-α lines. The transition is—among other parameters—dependent on pressure (15 Pa in our case). Discrimination between the E-, transitional and H-mode operations is possible from the temporal structure of the emission and from the intensity level. In the E- and transitional modes the intensity is about a factor of 100 less than in the H-mode. Furthermore, the E-mode is characterized by the evolution of one emission maximum per RF-cycle ($t_{RF} = 74$ ns), while in the H-mode discharge two emission maxima per RF-cycle are clearly visible. The single maximum of the E-mode is attributed to fast electrons expelled by the sheath building up near the coil once in an excitation cycle. In the H-mode two maxima can be clearly observed, which are brought about by the currents in the discharge induced twice per period (figure 4(*c*)). During the transitional mode the second emission maximum starts to build up, which results in a broadening in the capacitive emission maximum (figure 4(*b*)).

It is remarkable that the modulation of the emission in the ICP is much less pronounced—only about 20% (figure 5)—as compared to more than 90% modulation observed in the CCRF discharge [10].

The spatial intensity distribution is characterized by a gradual increase from the grounded electrode until the emission maximum is reached. In the H-mode the emission maximum is located closer to the antenna coil—about 3 mm below the upper observation limit (10 mm below

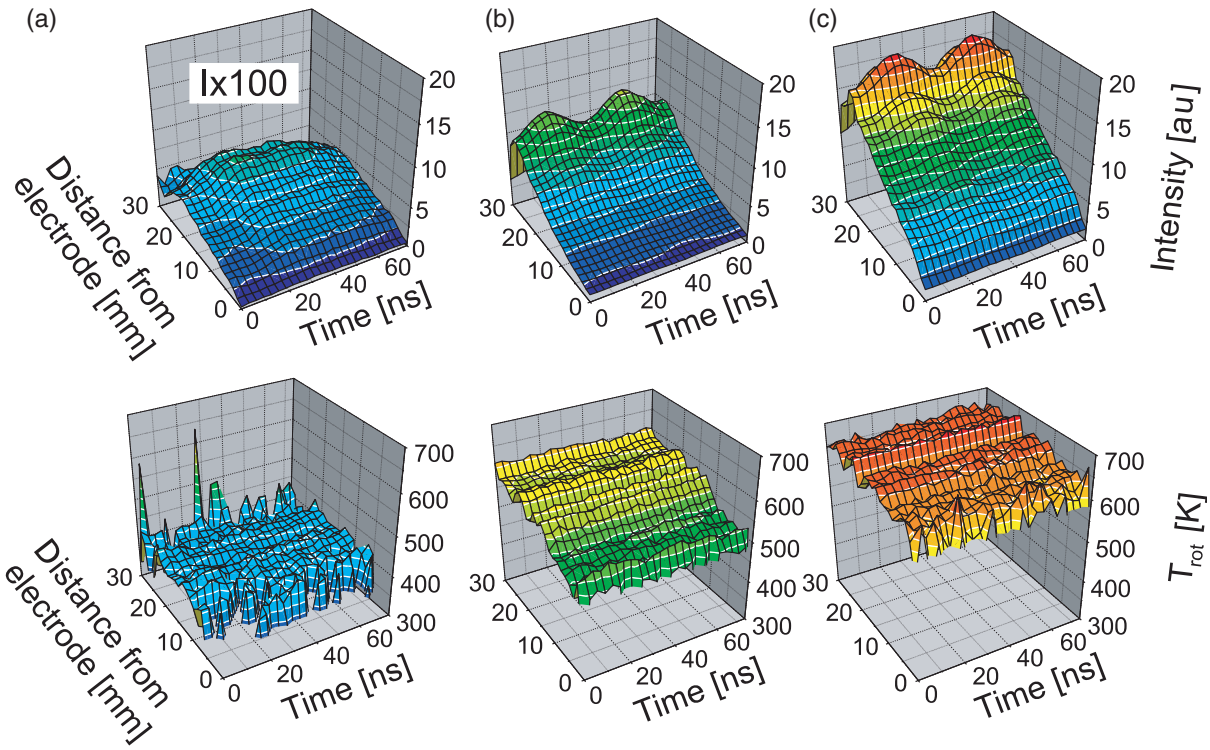

Figure 5. Temporal development of the axial emission intensity profile of the Q(1) line (top row) and of the rotational temperature profile (bottom row) at 15 Pa and for different input powers of (*a*) transitional mode (150 W), (*b*) H-mode (250 W) and (*c*) H-mode (350 W). The intensity in (*a*) was multiplied by a factor of 100.

the antenna coil)—as compared to 10 mm (17 mm) for the transitional mode.

The emission intensity rises with increasing power and changes abruptly to much higher values (up to two orders of magnitude) when the discharge changes to the H-mode as can be seen from figure 5. The intensity of the transitional mode (figure 5(*a*)) was multiplied by a factor of 100 in order to facilitate the comparison.

Under some conditions (low power, far away from the coil, near the cooled electrode) it was not possible to calculate a rotational temperature for E-mode discharges, because the emission was so faint that only three rotational lines or less could be safely recorded. Even with our fast camera the integration time would have been so long that one complete radial scan would have taken more than a day. Although the computer could process these spectra and yield a rotational temperature, we skipped these spectra since errors are large. For this reason, part of the rotational temperature near the grounded electrode is missing at low power (150 W) in the bottom row of figure 5 showing the temporal development of the rotational temperature along the discharge axis. In this and in the transitional mode the temperature assumes values in the range of 400 K in agreement with the results obtained before in a real CCRF discharge at similar power but higher pressure [10]. In the H-mode the rotational temperature rises near the coil from about 600 K up to a value of 650 K with increasing power from 250 to 350 W. At the same time, the temperature close to the electrode rises from about 500 to about 600 K at a power of 350 W. The temperature gradient between the coil and the electrode is reduced from about 100 K at 250 W to 50 K at 350 W.

4.2. Time dependences of rotational temperatures

As one very important observation from the time resolved rotational temperature measurement within one cycle of the ICP discharge, we note that the temperature does not exhibit any prominent time dependence on a time scale of the RF period ($\tau_{RF} = 74$ ns), in either of the discharge modes as displayed in the bottom line of figure 5. Note that the same analysis reveals a time dependent modulation of the rotational distribution, equivalent to about 100 K variation of the rotational temperature, in the case of a CCRF discharge [10]. In that case it can be shown that the time variation is correlated with the population out of high lying cascading states so that the conditions for the underlying model are fulfilled best at the excitation maximum. Then, the analysis yields the (formally) lowest rotational temperature.

One important difference between the CCRF discharge and the ICP is—as already mentioned—that the modulation of the emission intensity in the case of the CCRF discharge was high in comparison with the intensity modulation in the ICP discharge for our conditions.

To further analyse this behaviour, the analytical model of the former publication was replaced and extended by a numerical model based on the same assumptions as stated in [10]. In contrast to the analytical model starting from the condition of maximum excitation and running only up to the next exciting pulse the numerical model includes the periodic excitation due to the electrons driven by the RF generator. To describe the time behaviour of the excitation we chose a $\sin^2 \omega_{RF} t$-functionality for a 'synthetic' excitation function providing the necessary twofold excitation per RF-cycle in

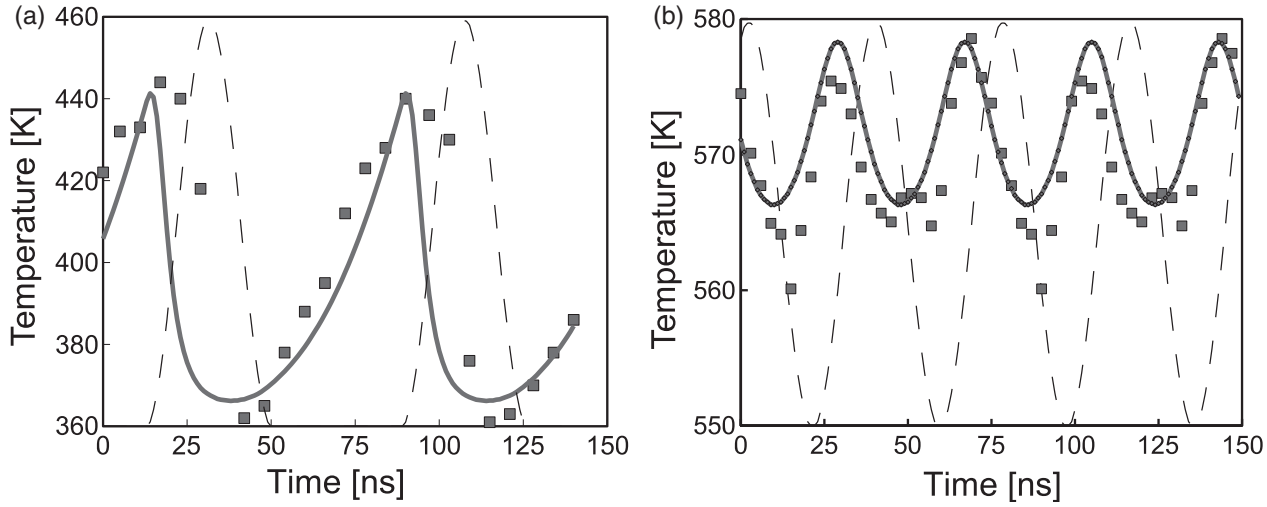

Figure 6. Modelling of the time dependent rotational temperature for (*a*) a CCRF discharge at 42 Pa and (*b*) for an inductively coupled RF discharge at 15 Pa in hydrogen. The continuous line displays the time dependence of the temperature calculated from the model. The squares show measured temperatures for the CCRF discharge at 100 W from [10] and for the ICP at 350 W from this work. Both measurements are made for the axial distance of maximum emission. The dashed lines show the respective assumed excitation functions. The bottom values of the temperature axes correspond to the initial gas temperatures given as starting conditions for the model, respectively.

H-mode. For the E-mode, the second maximum of the function within a cycle was arbitrarily set to zero. The behaviour is represented in figure 6 by dashed lines. The half-width of the excitation maxima of about 20 ns is in good agreement with the measurements. A constant lifetime of 143 ns for the cascading levels was used while for the Fulcher transitions the effect of collisional quenching was taken into account by introducing effective lifetimes. During the simulation, as a first step, the population of cascade and upper Fulcher levels is calculated neglecting the rotational sublevels until stationarity is reached. As a first result, it was found that within the model a contribution by the cascades of about 8% yields a modulation of the emission that agrees very well with the observed one for the H-mode as well as for the E-mode and for different pressures. This is in good agreement with the results of the analytical model. In a second step the population dynamics of the rotational sublevels is then taken into account. As an initial value, the population of the rotational ground state levels is set according to a given temperature. Note that this initial temperature corresponds to the gas temperature since equilibrium is assumed in the ground state. From here, the population and depopulation of upper Fulcher and cascade levels are calculated as described above. All cascade levels are equally weighted. The calculation runs through about 30 RF-cycles before the results become stationary. The resulting rotational distribution is finally correlated with a temperature.

As a test, the model was applied to the conditions of the capacitively coupled discharge as used by Gans *et al* [10]. The result is shown as a continuous line on the left-hand side of figure 6 in comparison to the temperature behaviour as measured by PROES (filled squares). Two RF-cycles are displayed on the time axis. The bottom value of the temperature axis marks the initial temperature of the calculation. The temperature rise after the end of the excitation pulse agrees well with the measured behaviour. Deviations for the time of the excitation pulse can be attributed to differences between the shape of the 'synthetic' and actual excitation function.

The right-hand side graph of figure 6 shows the calculated temperature behaviour for an inductively coupled hydrogen plasma at 15 Pa in combination with measurements taken at the point of maximum emission, about 10 mm below the coil. Again, the base line temperature corresponds to the initially assumed gas temperature for the model and two RF-cycles are plotted. Both graphs clearly demonstrate that the model describes well the time behaviour for both discharge types. During the excitation phase the rotational temperature falls quickly towards the given gas temperature since at that time the influence of the cascades is minimum. After this phase, the cascade contributions yield a change in the rotational distribution due to the long lifetime of the cascading levels. This is analysed as an (artificial) increase of the attributed rotational temperature. For the CCRF discharge due to the long time between excitation pulses the temperature variations are large ($\Delta T \approx 90$ K) since the relative contribution from the cascades increases because of the longer lifetime of these states. At the same time, the population of both levels has fallen so far, that it can be neglected compared to the population by the following excitation pulse. In this way, the temperature at maximum excitation is very close to the ground state gas temperature. Due to the more rapid repetition of the excitation in the ICP the variation of the relative contribution to the population is reduced, so that the temperature variations stay small—for our conditions resulting in temperature variations of about 20 K. On the other hand, the Fulcher states are not depleted as much as in the capacitive mode so that there is a continuous contribution resulting in a more pronounced deviation from the gas temperature as compared to the capacitive case. For our pressure range of 5–60 Pa this increase stays below 20 K. This means that both effects are within the estimated error of our temperature measurement. From the modelling, it can be assumed that quenching prevents a stronger deviation from the starting temperature under these

conditions but yields a stronger temperature modulation of about 50 K at 60 Pa. Intensity problems impede a verification of these structures in our discharge. The rise of the minimum rotational temperature as well as the modulation would assume higher values if the cascade contributions were stronger than mentioned above.

In conclusion, it can be stated that the effects described here influence the results of the common time-integrated OES analysis but the deviations will stay within typical experimental errors. Since the time dependence of the observed rotational temperature is so small, all of the following results will be time-integrated values.

4.3. Fabry–Perot interferometric measurement of the gas temperature

The discussion above immediately leads to the demand of an independent check of the gas temperature as determined by PROES. A technically challenging method would be the calculation from the measurement of the ground state line width by laser induced fluorescence. Much simpler and equally significant is the determination of the translational temperature on the basis of Fulcher linewidths. The Doppler-broadened linewidth amounts to about $\Delta\lambda_{FWHM} \sim 5$ pm at a gas temperature of 300 K. This value exceeds by far the resolution of the installed 2 m spectrograph/camera combination. The optical system was, therefore, extended by installing a Fabry–Perot interferometer (FPI; Burleigh RC-150) within the optical path in front of the entrance slit of the spectrograph. The interferometer is equipped with two plane plates of 50 mm diameter coated for red wavelengths. The plate distance was adjusted to 12 mm (see figure 1). In this combination, the spectrograph serves to select one free spectral range of the interferometer, which provides the necessary spectral resolution. In this arrangement only a cross section of the typical ring system of a FPI appears within one spectral line of the spectrograph on the camera. Since this dimension of the camera coincides with the axial dimension of the discharge, it is possible, in principle, to get spatially resolved information. In our experiment, this is limited by the available intensity at each location, so that, again, the position of maximum emission was used for the analyses. The finesse of the system was checked by analysing a He–Ne laser to exceed a value of 15 resulting in a resolution of <0.5 pm. The translational temperature is determined from the width of the Gaussian contribution of a Voigt profile fitted to the $v = 2$ Q(1) Fulcher-α line. The translational temperature of H_2 measured with this system is displayed in figure 7 as a function of the input power at a pressure of 15 Pa. The results are compared with the measurements from the analyses of the rotational Fulcher-α bands. For both cases, it is assumed that the temperatures reflect the gas temperature. Within the H-mode the temperature rises linearly from about 550 to 700 K for input powers between 250 and 400 W. The rotational temperatures are slightly higher than the translational ones, which might be attributed to the temperature deviation as explained above. Below 250 W, in E-mode, only the analysis of the rotational bands is available for intensity reasons. Here, a temperature of 400 K is measured. Both methods yield comparable results as demonstrated in figure 7. For the

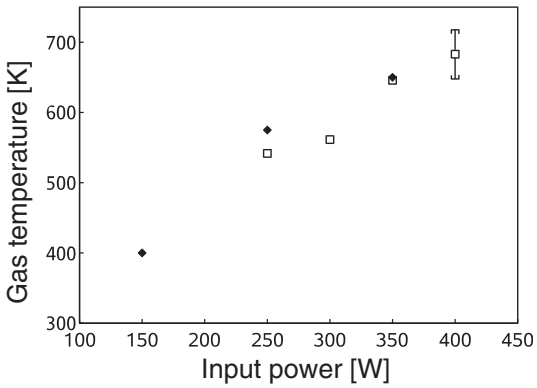

Figure 7. Power dependence of the gas temperature as determined from the analyses of rotational Fulcher bands (⧫) and from the Fabry–Perot interferometry (□) at a hydrogen pressure of 15 Pa at the point of maximum emission within the discharge. At 150 W the discharge is in the E-mode and the emission is too dim to allow interferometry.

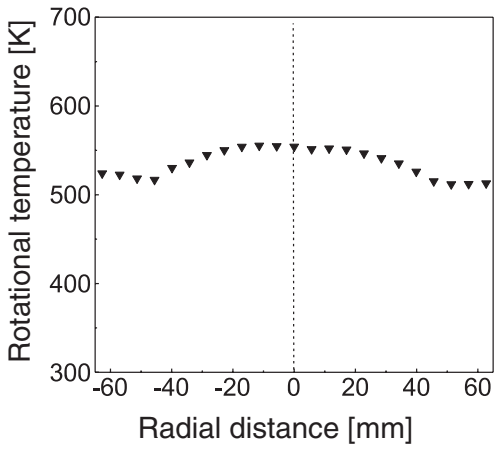

Figure 8. Radially resolved time and space integrated temperature profile of the discharge at 250 W and 15 Pa measured in the centre plane.

interferometric measurements we estimate the statistical error to be below 50 K.

From these measurements we conclude that temperature analyses from the rotational bands yields results that reflect the real gas temperature for our discharge.

4.4. Radial temperature results

Since the temporal variations of the temperatures are below 20 K and close to the noise level we will neglect time dependences in the analysis of the radially and axially resolved measurements. Figure 8 displays the time-integrated radially resolved temperature profile at 250 W and 15 Pa measured in the central plane of the discharge. For this experiment one complete radial scan through the whole discharge was performed and analysed separately for both sides from the discharge axis with the Abel algorithm. The symmetric property of the temperature around the centre of the discharge is clearly observable, so that radial symmetry as the most important prerequisite to applicability of Abel inversion is fulfilled.

The behaviour of two-dimensional axial and radial temperature profiles as a function of input power is shown in

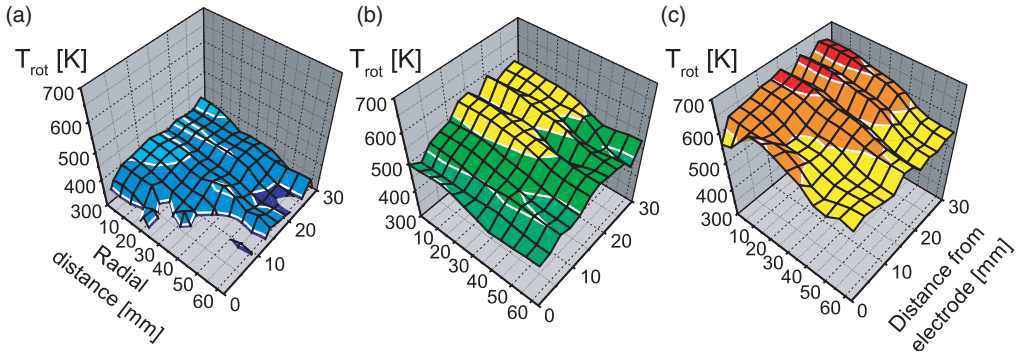

Figure 9. Time-integrated Abel inverted temperature fields at a pressure of 15 Pa as a function of power (*a*) transitional mode (150 W), (*b*) H-mode (250 W) and (*c*) H-mode (350 W).

figure 9. In a plateau region of about 35 mm radius a constant temperature is observed. For the H-mode measurements this region of constant temperature expands with increasing power further towards the electrode. In this region, the temperature shows a maximum value of about 400 K, 575 K and 650 K at powers of 150 W, 250 W and 350 W, respectively. The temperature decreases for each power towards the grounded electrode. For the transitional mode the temperature reaches about 350 K very close to the electrode. At 250 W the temperature falls off within about 10 mm from the plateau value to 450 K near the electrode. At 350 W this reduction is much less pronounced (about 50 K), so that the plateau nearly fills the volume between coil and electrode. The radius of this region is clearly correlated with the outer radius of the exciting planar coil of 37–40 mm (depending on the spiral structure). The main power input into the discharge takes place in the volume below the coil. For higher radial distances the temperature falls off. Outside the discharge defined by the diameter of the coil and electrode at about 60 mm from the axis it has values of about 350, 500 and 575 K for increasing values of power. At this edge position the temperature only shows a very weak axial dependence and approaches a constant value. The variations stay within a limit of about 25 K. The temperature here is probably connected to the vessel temperature. This also rises with input power, meaning that more energy is transported outside to the walls.

The axial temperature structures extending radially throughout the discharge visible in the plots are not understood so far. Trivial artefacts like nonlinear behaviours of the detection system have been checked and excluded.

For 150 W input power, in the E-mode, the axial and radial structures are very weak. Within our measuring errors of about 25–50 K—depending mainly on intensities and therefore highest under these conditions—we can only state a decrease towards the electrode. Radially the discharge shows no clear dependence, so that the temperature stays at the value on the axis.

5. Conclusions

We have demonstrated the possibility of phase and space resolved optical emission spectroscopic measurements of rotational temperatures in an inductively coupled RF discharge in hydrogen based on Abel inverted Fulcher line intensities. The analysis of the emission clearly reveals the different operation modes of the ICP. Other important results are that the modulation of the emission is much weaker than in a CCRF discharge of similar dimensions and that the time dependences of the rotational population distribution observed within an RF-cycle are much smaller. The emission behaviour as well as the temporal characteristics of the rotational temperature could be described by a numerical model taking into account the influence of cascade contributions from higher lying states of the hydrogen molecule. The model shows that for the ICP the rotational temperature variation is small compared to the capacitive case and that an offset of the rotational temperature appears for our conditions. The identification of the rotational temperatures with the gas temperatures was cross-checked by determination of the translational temperature by linewidth measurements with a combination of a FPI and a spectrograph. The measured temperatures agree very well. A rotatable mirror set-up allowed us to record the Fulcher Q-branch rotational band of H_2 and to measure side-on intensities needed for Abel inversion and determination of radially and axially resolved temperature profiles. Power variations revealed temperatures on the axis of up to 650 K at 350 W input power. The temperatures stay constant within a bulk of the radial dimensions of the exciting coil. This constant temperature extends further from the coil in the direction of the grounded electrode, with increasing power.

Acknowledgments

We thank Mrs C Fischer and Mr J Leistikow for technical assistance. One of the authors (MAR) wants to thank the Egyptian government for a personal study grant.

References

[1] Schulz-von der Gathen V and Döbele H F 1996 *Plasma Chem. Plasma Process.* **16** 461
[2] Rousseau A, Granier A, Gousset G and P Leprince P 1994 *J. Phys. D: Appl. Phys.* **27** 1412
[3] Gottscho R A and Miller T A 1984 *Pure Appl. Chem.* **56** 184
[4] Abada H, Chabert P, Booth J P, Robiche J and Cartry G 2002 *J. Appl. Phys.* **92** 4223
[5] Behringer K and Fantz U 1999 *Contrib. Plasma Phys.* **39** 411
[6] Gans T, Schulz-von der Gathen V and Döbele H F 2004 *Contrib. Plasma Phys.* **44** 535
[7] Surrey E and Crowley B 2003 *Plasma Phys. Control. Fusion* **45** 1209

[8] Lavrov B P 1980 *Opt. Spectrosc.* **48** 375
[9] Stamou S, Mataras D and Rapakoulias D 1998 *J. Phys. D: Appl. Phys.* **31** 2513
[10] Gans T, Schulz-von der Gathen V and Döbele H F 2001 *Plasma Sources Sci. Technol.* **10** 17
[11] Fantz U 2002 *Contrib. Plasma Phys.* **42** 675
[12] Schulz-von der Gathen V, Röpcke J, Gans T, Käning M, Lukas C and Döbele H F 2001 *Plasma Sources Sci. Technol.* **10** 530
[13] Cherigier L, Czarnetzki U, Luggenhölscher D, Schulz-von der Gathen V and H F Döbele H F 1999 *J. Appl. Phys.* **85** 696
[14] Lochte-Holtgreven W 1968 *Plasma Diagnostics* (Amsterdam: North-Holland) p 184
[15] Blades M W and Horlick G 1980 *Appl. Spectrosc.* **34** 696–9
[16] Blades M W 1983 *Appl. Spectrosc.* **37** 371
[17] Pretzler G 1991 *Z. Naturf.* a **46** 639
[18] Pretzler G, Jäger H, Neger T, Philipp H and Woisetschläger J 1992 *Z. Naturf.* a **47** 955
[19] Astashkevich S A, Käning M, Käning E, Kokina N V, Lavrov B P, Ohl A and Röpcke J 1996 *J. Quant. Spectrosc. Radiat. Transfer* **56** 725